SAND2015-8427J

Assessment of Saturation Changes Around Cavities and the Impact on Seismic Waves

Nedra D. Bonal[1] and Sharon L. E. Desilets[2]

[1]Sandia National Laboratories

Albuquerque, NM 87185-0750

Email: nbonal@sandia.gov

[2]Consultant

Albuquerque, NM 87106

Email: seinloth@gmail.com

ABSTRACT

According to theory, seismic methods should be able to identify cavities. The high impedance contrast between the rock (fast velocity, high density) and the air (slow velocity, low density) should produce strong reflections and refractions off cavity walls. In practice, however, cavities are not always easily detected. Changes in pore saturation, fracturing, and stress near the wall of the cavity may decrease the impedance contrast and diffuse the rock/air interface. To determine the impact of these effects on seismic waves, we first aim to understand the hydrological processes in the medium surrounding the cavity, a tunnel in this case. We simulate flow through the vadose zone to provide insight into how a cavity alters saturation. Next we examine how this saturation affects seismic velocities. Finally, we use a wave propagation code to simulate seismic waves through the saturation models. Results are presented from hydrology models for three cases: the tunnel far above the water table, the tunnel just above the water table and within the capillary fringe, and the tunnel below the water table with the tunnel being drained. We also present the results of seismic wave propagation through these models to determine the impact these effects have on seismic waves.

Introduction

Detecting tunnels using surface seismic techniques has been problematic despite the large impedance contrast expected from the air-rock interface. Seismic reflection and refraction have been viewed as some of the better methods to detect tunnels but in practice, results are not always as good as expected from theory (Engelsfeld *et al.*, 2008, Engelsfeld *et al.*, 2011, Grandjean and Leparoux, 2004, and Symons *et al.*, 2009). This poor ability to detect tunnels using seismic methods may be due to the effects constructing a tunnel has on rock properties, fractures, and pore fluid content near the air-rock interface, referred to as the halo. Clandestine tunnels like those at border crossings are often constructed in weak rock and near the water table, where saturation of pore spaces may vary due to capillarity and other effects such as pressure and pore size. Effects of tunnel construction in the near surface environment produce a lower impedance contrast than in competent rock.

To determine the impact tunnel construction has on seismic waves, we first simulate flow through models of the subsurface to examine saturation changes due to a cavity and the halo around the cavity. Next we convert water content from the results of flow simulation to seismic velocities using a combination of Biot-Gassmann's and Brutsaert's (1964) fluid substitution equations. The Biot-Gassmann theory is typically used to predict velocities from variant saturation in rocks. However, in poorly consolidated, shallow media, this theory tends to over-predict velocities. Brutsaert's (1964) theory is based on that of Biot but also accounts for capillary pressure and more accurately predicts velocities in poorly consolidated, shallow media. We use Brutsaert's theory for the poorly consolidated, shallow material and the tunnel halo. We use the Biot-Gassmann theory for more consolidated, deeper materials to predict seismic velocities from our saturation models. Next, we use a wave propagation code to simulate seismic waves through these seismic velocity models.

Hydrology Modeling

To assess the potential for identifying underground tunnels with seismic tools, it is necessary to consider the hydrology of the subsurface. This work uses HYDRUS-2D to examine flow patterns around a tunnel. HYDRUS is a FORTRAN code that numerically solves the Richard's equation for variable saturation using finite elements. Our domain is a vertical slice of subsurface that is 50 m wide and 30 m deep. The cross-section of the tunnel is modeled as a keyhole shape with a width and height of 1 and 1.5 m, respectively. A 'halo' region of graduated higher conductivity representing damage from tunnel construction surrounds the opening. The top of the tunnel is 13.5 m below the surface. **Error! Reference source not found.** shows the model domain and finite element mesh. The mesh, generated by HYDRUS, contains smaller elements in the area of the tunnel for optimum resolution of the hydrology in that region.

The soil matrix has been modeled with three layers. **Error! Reference source not found.** shows the soil properties used in the Hydrus modeling for these layers and for the halo region. Layers were initially selected to match well log observations from the Otay Mesa area of southern California (Ninyo and Moore, 2007). The center layer was then modified from a siltstone to clay loam in order to maximize the possible effects of hydrology around the tunnel. The top layer is unconsolidated loam, the middle layer is a semi-consolidated clay loam, and the bottom is a semi-consolidated sand/sandstone. In the halo region, the soil properties are graduated from a coarse-fractured, higher-conductivity medium (Halo 1) toward the background clay loam. The colored nodes in the right image of **Error! Reference source not found.**B correspond with the soil properties designated as Halo 1 (yellow node) through Halo 5 (light blue node) in **Error! Reference source not found.**.

For this domain, three cases are considered: tunnel in the vadose zone with a deep water table, tunnel in the vadose zone close to the water table, and tunnel in the saturated zone. The top and side boundary conditions are the same for each of these three cases. The boundary at the top of the domain is atmospheric, which allows for a prescribed time-variable schedule of precipitation and evaporation. The sides of the domain are zero flux. The tunnel boundary is a seepage face, a system-dependent condition

that sets the boundary to a constant head of zero when saturated, and zero flux when unsaturated. The code assumes that water crossing the boundary is immediately removed from the system (*e.g.* in this case by pumping from the tunnel). The bottom boundary is set to free drainage for the unsaturated case with the deep water table and to constant pressure head for the other two cases.

The initial condition is defined in terms of pressure head. HYDRUS allows a method of assignment where the pressure head for the bottom boundary is user-defined and it calculates an equilibrium distribution of pressure for all the nodes above the bottom boundary. Using this approach, we assigned pressure heads for the bottom boundary that would correspond with the desired water table position for each case. Therefore, the bottom value is set to 10 m and 20 m of pressure for the tunnel near above and tunnel below the water table cases, corresponding to a water table at 20 m and 10 m below the ground surface, respectively. Above the water table, and for the far above case, the initial head is set as a constant at -1 m pressure.

Atmospheric forcing was defined as a simplified southwestern meteorological pattern (Adams and Comrie, 1997) with a heavier summer monsoon season, lighter but longer winter wet season, and dry periods in between (Figure 2). Precipitation initiates immediately at a rate of 0.00635 m/day for 30 days, followed by 60 days of no precipitation, then 150 days of precipitation at a rate of 0.00127 m/day and finally another dry period of 125 days. The entire simulation is run for 3 years. No evaporation or transpiration is considered.

Hydrology Results

Results have been calculated for these three hydrological cases, considering a tunnel with and without a halo region of increased fracturing and therefore increased hydraulic conductivity. For the tunnel far above a water table, differences can be seen in time and between cases. For the tunnel without a high-conductivity halo (Fig. 3A), water draining in the system moves around the tunnel such that a region of higher water content develops as lobes above and along the sides of the tunnel. In addition, a shadow

effect of lower water content occurs below the tunnel as the infiltration front passes. These enlarged regions of higher and lower water content, here approximately triple the size of the tunnel, increase the tunnel's footprint and may improve detection by seismic methods. For the same tunnel far above the water, but adding a high-conductivity halo region (Fig. 3B), the flow patterns change. Within the halo the higher water content lobes and lower water content shadow are apparent; however, the high-conductivity of the halo allows water to flow through that region preferentially such that the opposite pattern is observed outside the halo: lower water content lobes develop above and beside the halo, and higher water content area develops below. In both cases saturation is not achieved around the area of the tunnel during the simulation and so no water drains across the seepage face.

The results for the tunnel above a near water table are initially similar to those above a much lower water table. With time (t = 876 days), a quasi-steady state condition is reached with water moving down through the system and the relation to the water table (Fig. 4). Again, the halo region of high-conductivity allows water to move preferentially around the outside of the tunnel, and creates a larger footprint for observing seismic velocity changes. All remaining hydrology models are shown at quasi-steady state conditions at t = 876 days.

The results for the tunnel below the water table show that the tunnel acts as a drain to locally depress the water table (Fig. 5). This draining should significantly enhance the change in seismic velocities to help locate the tunnel. While the effect is more dramatic in the case with the halo because of the higher conductivity region, this difference is not as large as the overall effect of the drain.

Seismic Velocity Calculation

Hydrology results were incorporated into the seismic velocity calculation. Two different methods were used to best represent unconsolidated and semi-consolidated conditions: Brutsaert (1964) and Biot-Gassmann relation, respectively. Brutsaert's equations describe the near-surface sound velocity as a function of water content. This approach best estimates velocities where the matric potential is important

relative to the overburden; we applied it to all soil with depth less than 5 m, and also to the highly fractured halo region. In this case,

$$v_p = \left[\frac{0.306 a p_e^{1/3} \left\{ 1 + \frac{30.75\left[(1-S)K_g + SK_l\right]^{3/2} b}{p_e^{1/2}} \right\}^{5/3}}{\rho_m \phi b^{2/3} \left\{ 1 + \frac{46.12\left[(1-S)K_g + SK_l\right]^{3/2} b}{p_e^{1/2}} \right\}} \right]^{1/2} \tag{1}$$

where v_p is acoustic velocity, S is saturation, p_e is effective pressure in the medium, ρ_m is the bulk density, ϕ is the porosity, K_g and K_l are the bulk modulus of gas and liquid, and a and b are estimated elastic constants.

The remaining portions of the subsurface were calculated with the Biot-Gassman equation. For this approach, the saturated bulk modulus, K_{sat}, was determined using a form of Gassmann's equation:

$$K_{sat} = K_{dry} + \frac{\left(1 - \frac{K_{dry}}{K_o}\right)^2}{\frac{\phi}{K_{fl}} + \frac{(1-\phi)}{K_o} - \frac{K_{dry}}{K_o^2}} \tag{2}$$

where K_{dry} is the dry bulk modulus of the medium, K_o is the mineral bulk modulus, and K_{fl} is the bulk modulus of the fluid (air and water) in the pore space. K_{dry} and K_o were determined from literature values for the materials assumed in the hydrology models. K_{fl} was calculated for partial saturation using the Reuss (1929) average:

$$\frac{1}{K_{fl}} = \sum \frac{S_i}{K_i} = \frac{S}{K_l} + \frac{(1-S)}{K_g}$$

Velocity (v_p) is calculated as

$$v_p^2 = {}^1/_\rho \left[K_{sat} + {}^4/_3 \mu_{sat}\right]$$

where μ_{sat} is the saturated shear modulus of the rock frame which is assumed to equal the dry shear modulus of the rock frame (μ_{dry}) and ρ is the mineral density. Parameter values were selected from literature to best represent the soil type and shallow depth of the domain. K_{dry} and ϕ are specific to the subsurface layers and the halo sections (Table 1). The remaining parameters are constant across the entire domain (Table 2). Saturation is determined from the HYDRUS simulations.

Velocity Results

Seismic velocity was determined for all of the cases described in the hydrology section, and the results are grouped by the location of the water table. Figures 6-8 show contours of velocity magnitude as well as the fractional difference in velocity ($Dv/v_{no\ cavity}$) between the tunnel and no-tunnel cases. The velocity differences are bi-modally distributed: the structural variations in the halo region affect a larger velocity difference while, outside of a halo region, the differences result from water content variation and are three orders of magnitude smaller than those observed in the halo region. In order to visually capture all of the variations we constructed two sets of contours. The bottom sets of contours in each region consider only fractional difference values below 0.005.

For the above water table case, the small-scale velocity variations (Fig. 6, bottom) closely match the changes observed in the hydrology results (Fig. 3). The increase in water content around the top and sides of the no-halo tunnel (Fig. 6, left) correspond with a slight decrease in velocity in the same region. And the decrease in water content below the tunnel corresponds with a slight increase in velocity. When including the small-scale effects, the footprint area is nine times larger than the tunnel alone. For the case of a tunnel surrounded by a high-conductivity halo (Fig. 6, right), the halo region shows much greater velocity change (65%). This is due largely to the effect of the material differences (lower bulk modulus), which outweigh the increase in velocity expected to accompany the decrease in water content. Outside the halo region, the lobes of lower water content correspond with a slight increase in velocity. The higher

water content below the tunnel corresponds with a slight decrease in velocity. The halo itself triples the areal extent of higher-order velocity change. Including the lower-order areas affected, the impact of hydrology on the seismic velocity increases the total footprint to 54 times the size of the tunnel.

The results for the tunnel above a near water table (Fig. 7) are similar in pattern to that for the far-above case. Areas of increased and decreased water content around the no-halo tunnel show slight decreases and increases in velocity, respectively. The area affected is five times that of the area of the tunnel alone. The halo itself shows a much larger velocity change (65%) due to its altered structural properties, and the hydrology-affected change around the halo is 17 times larger than the tunnel. The proximity of the water table does not significantly change the areal extent of the velocity-disturbance footprint, except that the region of slight velocity change below the tunnel in the previous case is obscured by the water table here.

For the case where the tunnel is located below the water table (Fig. 8), the tunnel acts as a sink draining the water. The region drained shows the most significant higher-order changes in velocity due to the large change in water content. The size of this effect would increase as the depth of the tunnel below the water table increases. The halo region still shows significant velocity changes as well, with the greatest change (69 %) occurring in the part of the halo above and beside the tunnel.

Seismic Modeling

Synthetic seismograms were simulated using a parallelized three-dimensional (3D), anelastic wave propagation software called Parelasti developed by Sandia National Laboratories. It solves the linearized coupled set of elasto-dynamic partial differential equations using finite-difference approximations that are second order accurate in time and fourth order accurate in space. These simulations utilize the velocity-memory-stress description of these equations.

A convolutional perfectly matched layer (CPML) decreased instabilities at the boundaries of the model. A delta function force source was used for these simulations to represent a standard impact source

such as a sledgehammer or automatic weight drop. A Berlage (1932) wavelet modeled after Aldridge (1990) was used as the source time function to convolve with the force source simulations to produce traces similar to field data for comparison. Figure 9 shows an example of the Berlage wavelet used to create the synthetic seismograms. All wavelets are normalized to unit maximum absolute amplitude with main frequency = 60 Hz, time exponent n = 0.5, and initial phase angle = -90°. Artifacts at high contrast boundaries were smoothed using two-dimensional averaging over a window of specified size. A free surface made up of zeros 3 grid nodes deep was added to the top of the model to act as an absorbing boundary to prevent unrealistic reflections from the free surface.

Data were modeled to represent a linear refraction style survey with source locations spaced every 5 m along the surface of the modeled space from 5 m to 45 m. Source locations at 2 m and 48 m were also collected to get data at far offsets and spacing was reduced to 1 m between 20 m and 30 m to increase resolution near the tunnel. Three component receivers were spaced at 0.5 m intervals starting at 1.25 m and ending at 48.75 m and were buried 1 m below the ground surface to decrease noise. This configuration prevented sources from being located on top receivers.

Input for this simulation code includes P-wave velocity (Vp), shear-wave velocity (Vs), and density (r). Vp was obtained from the water content results from the Hydrus models described above. The results were then expanded in one dimension to create a pseudo-3D volume. Vs was obtained by multiplying the values in Vp by 0.4, which is typically used to represent near surface velocities. Density, r, was obtained using the standard Gardner's relation (Gardner *et al.*, 1974), $r = a*Vp^b$, where r is in Kg/m^3, a = 0.31, b = 0.25, and Vp was obtained as described above. An example of a shot gather from these simulations is shown in Fig. 10.

Synthetic Wave Propagation Results

Results of the synthetic seismograms described above show that the halo decreases the impedance contrast between air/rock interface for the far above and near water table cases. This decrease is not

significant enough to completely mask the tunnel however. Figures 11 and 12 show single traces through the no tunnel, tunnel with no halo, and tunnel with halo models for each of the three cases relative to the water table (figure columns A, B, and C). The top rows are seismic rays that have not passed through the tunnel or halo area. The middle rows are seismic rays that have passed through the tunnel (and halo) area relatively near the tunnel. The bottom rows are seismic rays that have passed through the tunnel (and halo) area at farther offsets. The tunnel is centered in the model at 25 m (about Trace number 50) and is at 14.5 m and 7.5 m depth below ground surface for Figs. 11-12, respectively. The source is located at 5 m (about Trace number 10). In columns A and B of Figs. 11-12, the presence of the halo slightly alters the amplitudes of the waves at near offsets (top rows) and alters the character of the waveform after the wave passes the tunnel location (middle and bottom rows). The presence of the tunnel without the halo has relatively minor effects on amplitudes and waveform character. For the below water table case (Figs. 11-12, column C), pumping water out of the tunnel draws down the water table locally above the tunnel. This results in significant changes in amplitudes and arrival times both with and without the presence of the halo though the halo increases these effects. The waveform character is altered at large offsets (bottom rows). The presence of the tunnel without the halo is more similar to the tunnel with halo case than the no tunnel case for the models with tunnels below the water table.

Conclusions

In general, the hydrology response to a no-halo tunnel increases the spatial area of velocity disturbance by approximately an order of magnitude compared to the spatial area of the tunnel without considering changes in saturation. However, the magnitude of these velocity changes when considering hydrology is three orders of magnitude smaller than that due to adding a tunnel to a previously uniform medium. The effect of a modeled halo region of higher conductivity further increases the entire footprint. Inside the halo region, the magnitude of velocity decreases approximately 700 m/s; this is 65% greater than due to adding a tunnel to a previously uniform medium. Immediately outside the halo, the hydrology

affects a smaller-order velocity disturbance with spatial area one order of magnitude larger than the size of the halo region. In the far above and near water table cases, this is a significant spatial increase, which may bring the entire disturbance within the detectable range of available seismic methods. In the below water table case, the draining of the water table from the tunnel causes the largest increase in footprint, present both with and without a halo considered. Because the hydrology effects outside the halo produce such low velocity variations, possibly on the order of natural medium heterogeneities, the presence of a high-conductivity halo, which is expected to be the more realistic case, may be key to distinguishing cavities from natural variability in the soil. For cases where the tunnel is located above the water table, the effects of the cavity without a halo closely resemble the effects if no tunnel is present. But the effects of the cavity with a halo are more easily discernable from the no tunnel cases. Therefore, the halo area has a more significant impact on seismic waves than the void itself. So identifying changes in material properties rather than voids within the material may be a better way to locate cavities.

Acknowledgements

Sandia National Laboratories is a multi-program laboratory managed and operated by Sandia Corporation, a wholly owned subsidiary of Lockheed Martin Corporation, for the U.S. Department of Energy's National Nuclear Security Administration under contract DE-AC04-94AL85000.

References

Adams, D.K. and Comrie, A.C., 1997, The North American Monsoon, Bulletin of the American Meteorological Society, **78**, 2197-2213.

Aldridge, D.F., 2000, Radiation of elastic waves from point sources in a uniform hole-space, Sandia Report SAND2000-1767, Sandia National Laboratories, Albuquerque, NM, 71 pp.

Aldridge, D.F., 1990, The Berlage wavelet, Geophysics, **55**, 1508-1511.

Bartel, L.C., Aldridge, D.F., Symons, N.P. and Haney, M.M., 2008, Reverse-time seismic and acoustic wave propagation: High-fidelity subsurface imaging, Sandia Report SAND2008-0159, Sandia National Laboratories, Albuquerque, NM, 54 pp.

Berlage, H.P., Jr., 1932, Seismometer, Handbuch der Geophysik, **4**, 299-526.

Biot, M.A., 1956. Theory of propagation of elastic waves in a fluid saturated porous solid: I. Low-frequency range, Journal of the Acoustic Society of America, **28**, 168–178.

Brutsaert, W., 1964, The propagation of elastic waves in unconsolidated unsaturated granular mediums. Journal of Geophysical Research, **69**, 243–257.

Engelsfeld, T., Sumanovac, F., and Pavin, N. 2008, "Investigation of underground cavities in a two-layer model using the refraction seismic method." Near Surface Geophysics, **6**(4), 221-231.

Engelsfeld, T., Sumanovac, F., and Krstić, V., 2011, Classification of near-surface anomalies in the seismic refraction method according to the shape of the time–distance graph: A theoretical approach. Journal of Applied Geophysics, **74**, 59–68.

Gardner, G.H.F., Gardner L.W., and Gregory A.R., 1974, "Formation velocity and density -- the diagnostic basics for stratigraphic traps". Geophysics, **39**, p. 770–780.

Gassmann, F., 1951, "Elastic waves through a packing of spheres". Geophysics, **16**(4), 673–685.

Grandjean, G., Leparoux, D., 2004. The potential of seismic methods for detecting cavities and buried objects: Experimentation at a test site. Journal of Applied Geophysics, **56**(2), 93–106.

Ninyo and Moore, 2007, Preliminary Geotechnical Study, Geotechnical and Environmental Sciences Consultants, Report CALTRAN/SR-11, San Diego, CA.

Reuss, A., 1929, Berechnung der Fliessgrenzen von Mischkristallen auf Grund der Plastizitatsbedingung fur Einkristalle, Zeitschrift fur Angewante Mathematik und Mechanik, **9**, 49-58.

Sobolik, S.R. and Bartel, L.C., 2010, Preliminary studies of tunnel interface response modeling using test data from underground storage facilities. Sandia Report SAND2010-7425, Sandia National Laboratories, Albuquerque, NM, 44 pp.

Symons, N.P., Abbott R.E., Bartel, L.C., Bonal N.D., Doser, A.B., Hollister, S.P., Klise, G.T., Nguyen, H.D., and O'Rourke, W.T., 2009, Border Tunnel LDRD, Sandia Report SAND2009-0631, Sandia National Laboratories, Albuquerque, NM, 199 pp.

Table 1. Hydrological properties of domain layers, including graduated halo.

	θr	ϕ	a [m-1]	N	Ks [m.d-1]	Kdry [Gpa]
Loam	0.078	0.43	10	0.2	0.2496	0.37
Sand	0.02	0.417	13.8	0.592	5.04	4
Clay Loam	0.075	0.39	3.86	0.194	0.0552	4
Halo 1	0.02	0.5	5	0.67	17.5	3.5
Halo 2	0.035	0.475	4.75	0.67	15	3
Halo 3	0.05	0.45	4.5	0.67	12.5	2.5
Halo 4	0.06	0.425	4.25	0.67	10	2
Halo 5	0.07	0.4	4	0.67	7.5	1.5

Table 2. Parameters for Brutsaert and Biot-Gassman calculations.

Kg	0.00014	GPa
Kl	2.2	GPa
a	1	
b	1.0 x 10-20	GPa
rl	1000	kg m-3
rs	2650	kg m-3
mdry	3	GPa
Ko	39	GPa

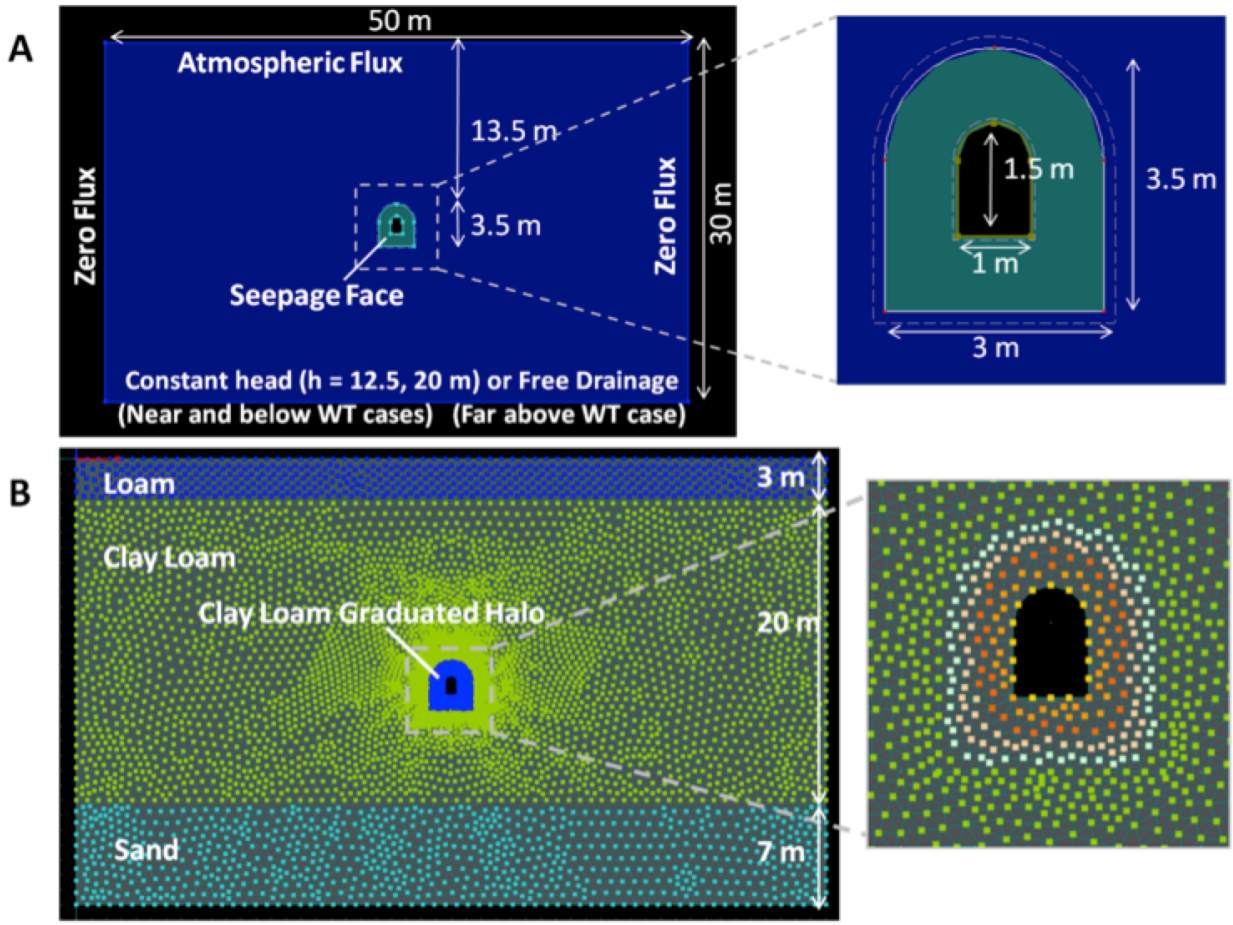

Figure 1. Model domain showing (A) peripheral and keyhole dimensions and boundary conditions, and (B) the finite element mesh with a fine-mesh and halo region around tunnel, and three material layers. The colored nodes in the halo show the graduated assignment of soil properties, moving from a coarse-fractured medium at the tunnel edge to background values for clay.

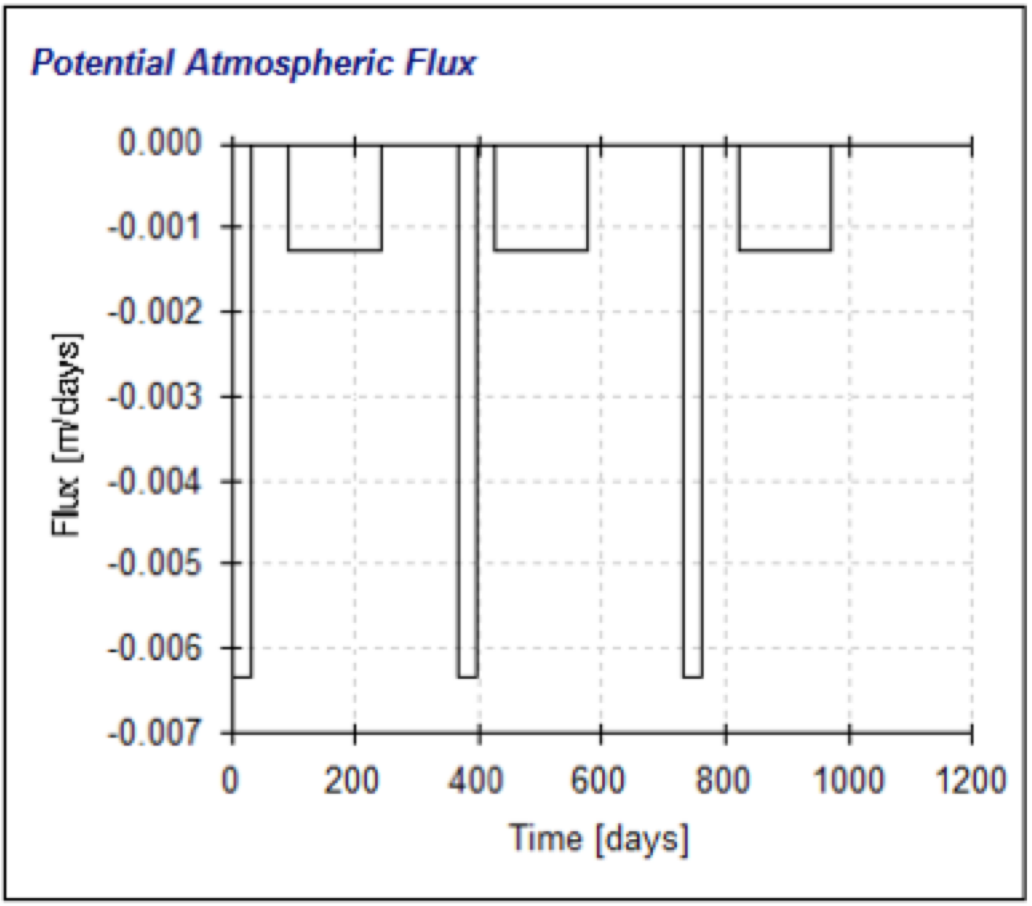

Figure 2. Southwestern monsoonal forcing pattern applied to atmospheric boundary condition.

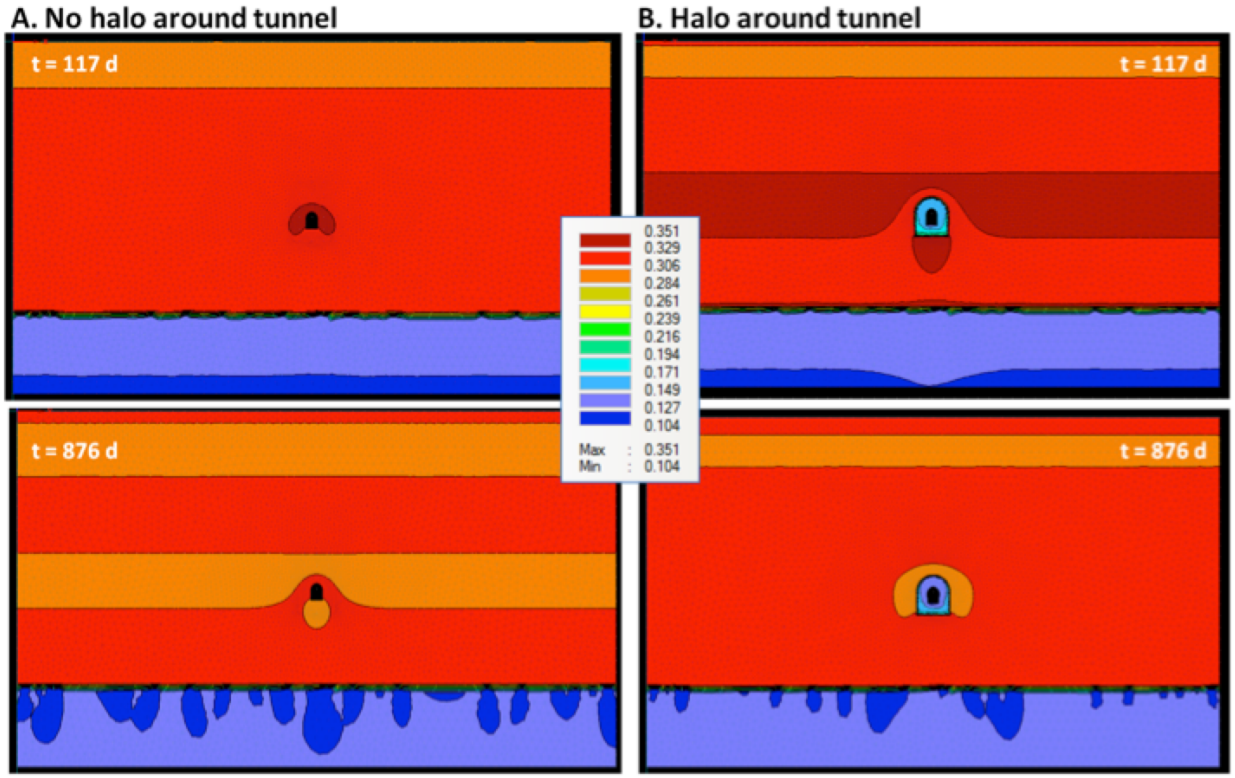

Figure 3. Results of water content at t = 117 and 876 days (top and bottom rows, respectively) for a tunnel far above the water table, comparing the cases with and without a halo around the tunnel, with the tunnel being far above the water table.

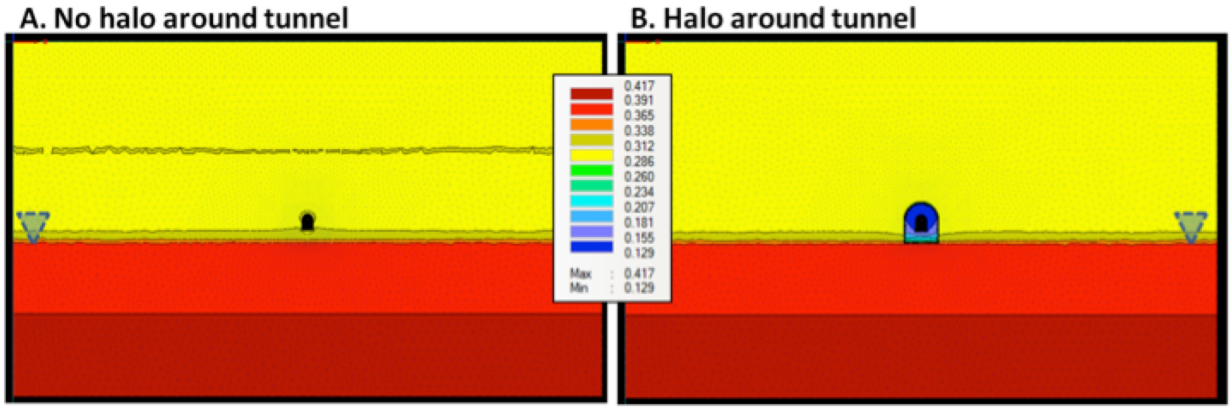

Figure 4. Results of water content for a tunnel above a near water table, comparing the cases with and without a halo around the tunnel. The capillary fringe region rises to the base of the tunnel.

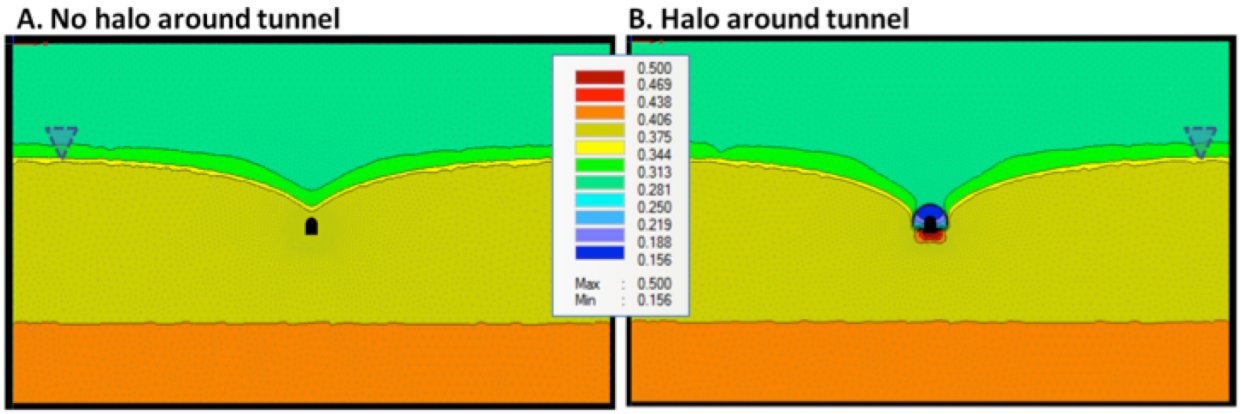

Figure 5. Water content for case of a tunnel below the water table, comparing the cases with and without the halo. The tunnel has drained the aquifer in the area of the tunnel.

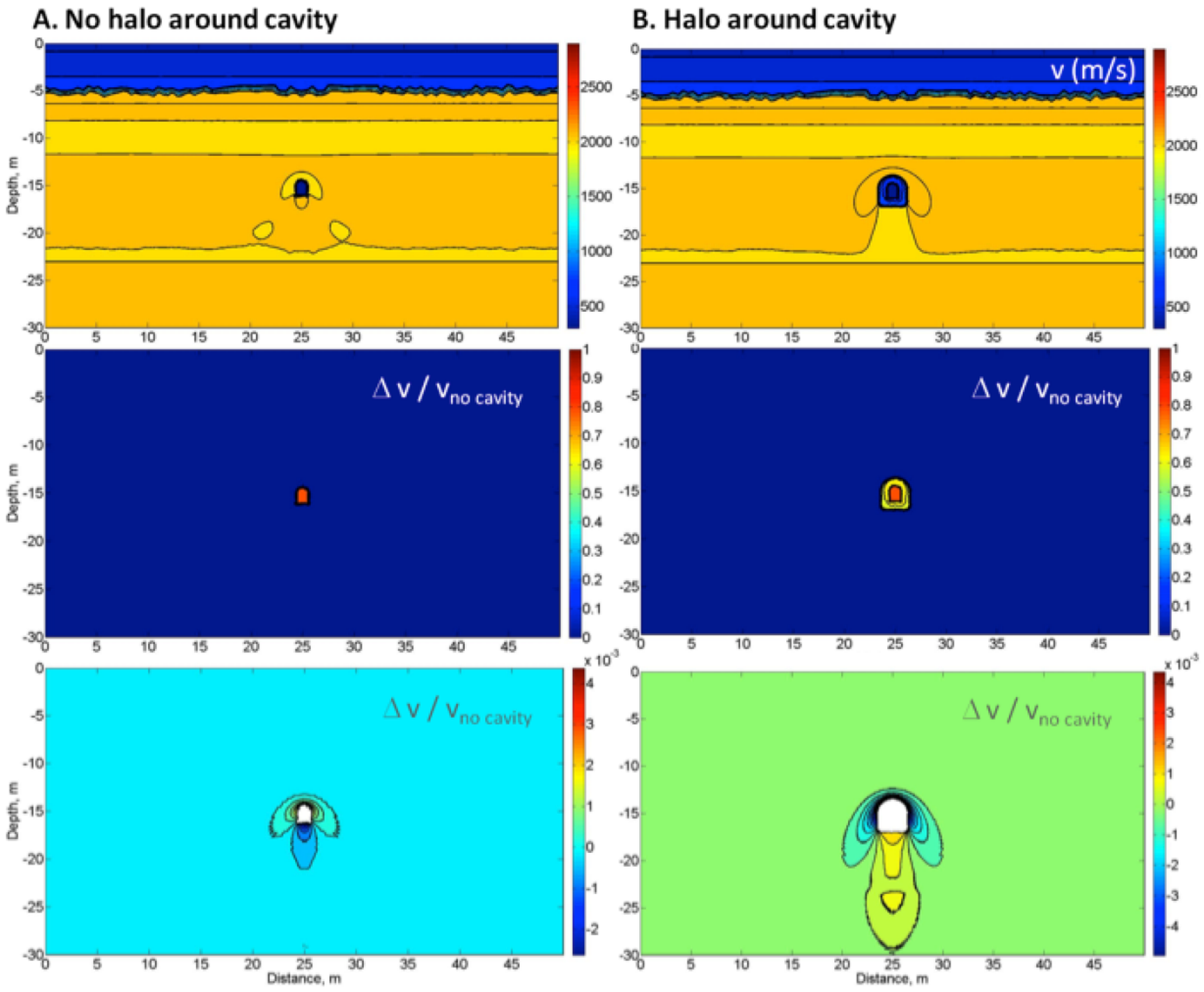

Figure 6. Velocity contours (top) and fractional velocity difference contours showing large-scale structural effects (middle) and smaller-scale hydrology effects (bottom) for the far-above water table case.

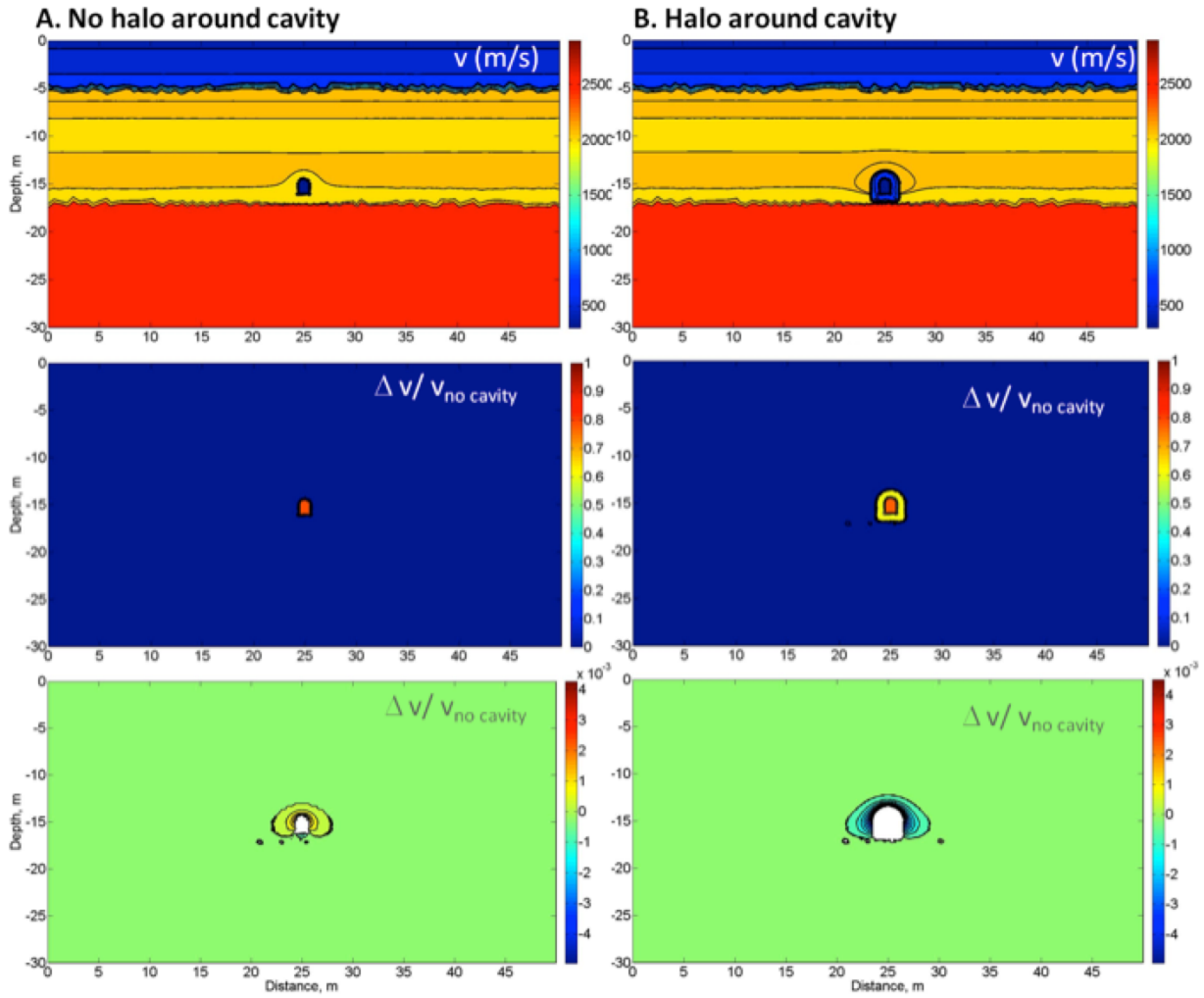

Figure 7. Velocity contours (top) and fractional velocity difference contours showing large-scale structural effects (middle) and smaller-scale hydrology effects (bottom) for the near-above water table case.

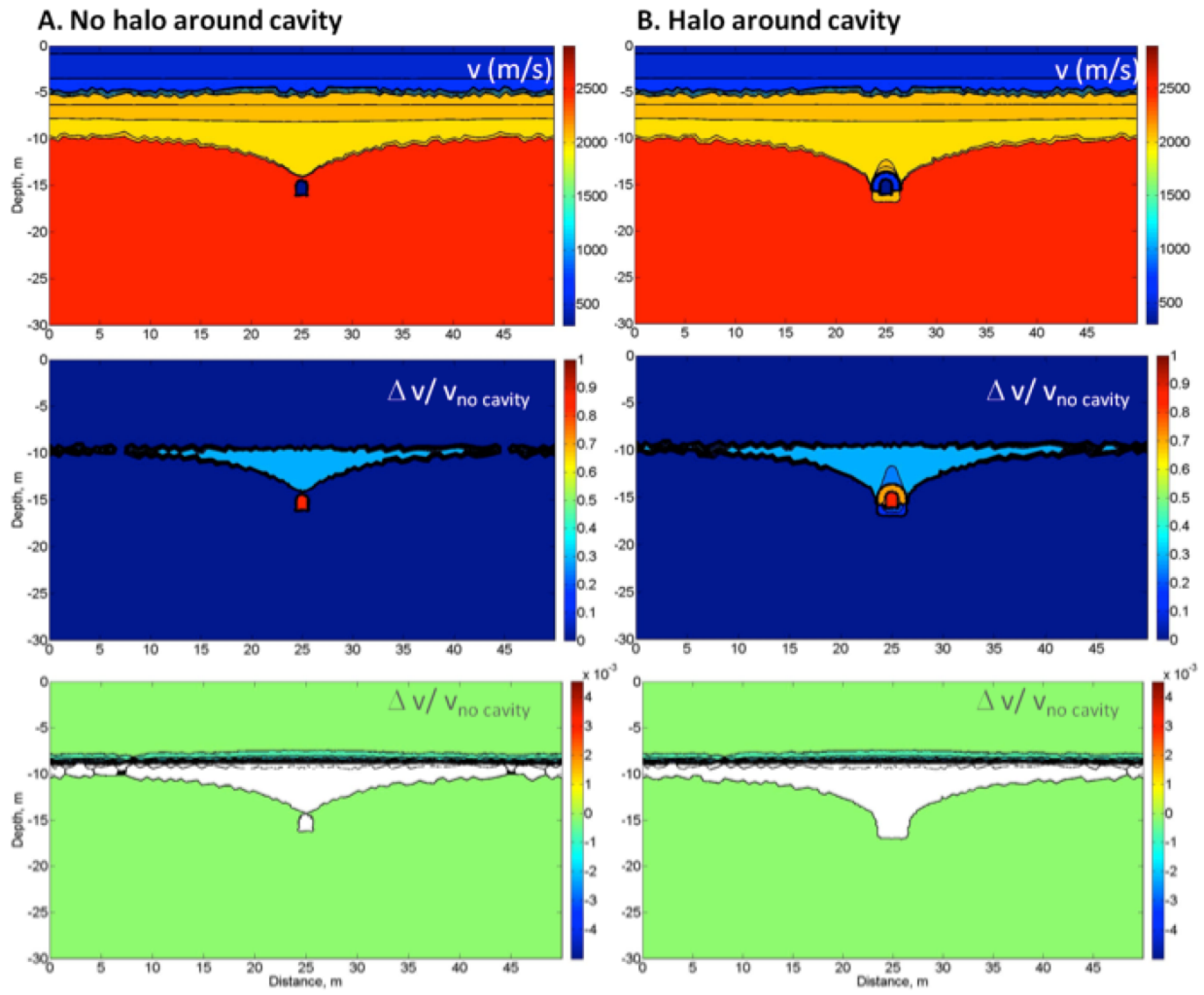

Figure 8. Velocity contours (top) and fractional velocity difference contours showing large-scale structural effects (middle) and smaller-scale hydrology effects (bottom) for the below water table case.

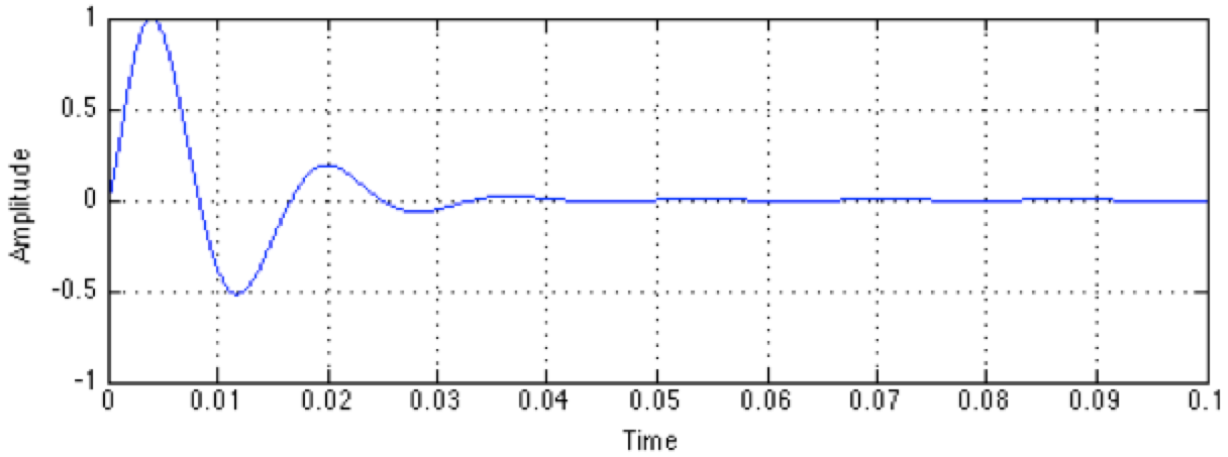

Figure 9: Example of the Berlage wavelet used as the source time function to create synthetic seismograms.

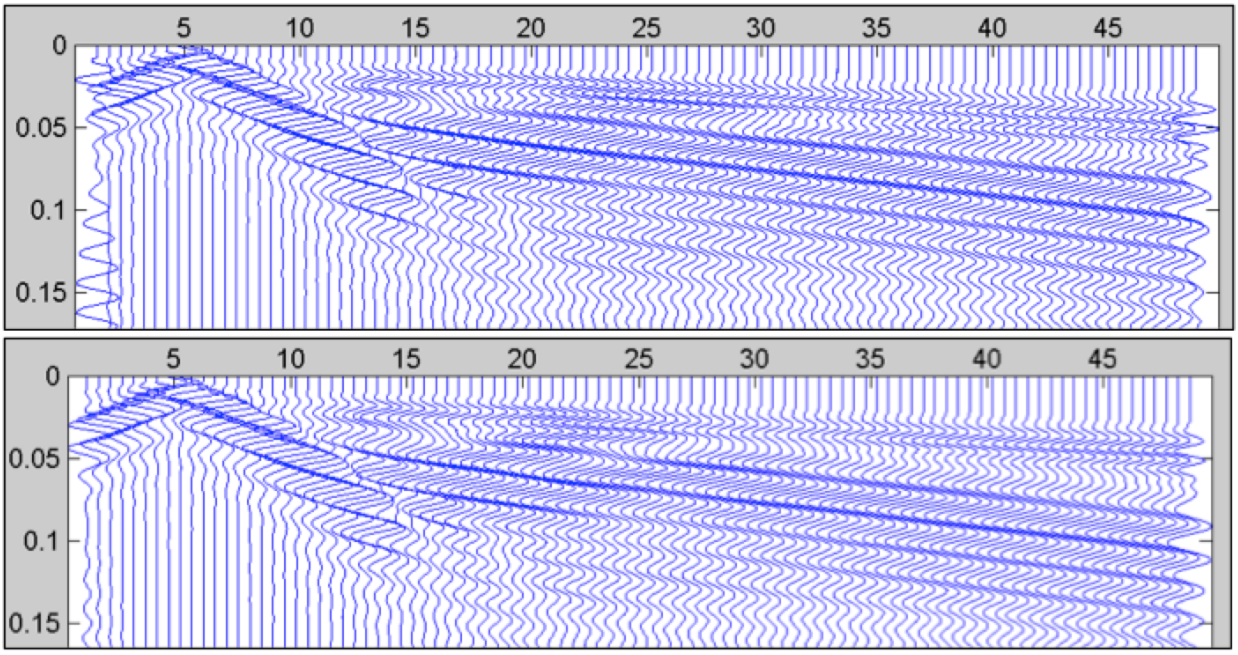

Figure 10: Examples of synthetic seismograms for the case where the tunnel is located far above the water table. The sources located at 5 m. The x-axes are distance in meters and the y-axes are time in seconds. The top figure does not contain a tunnel and the bottom figure is for the case shown in Fig. 6B, where a high conductivity halo is present around the tunnel cavity.

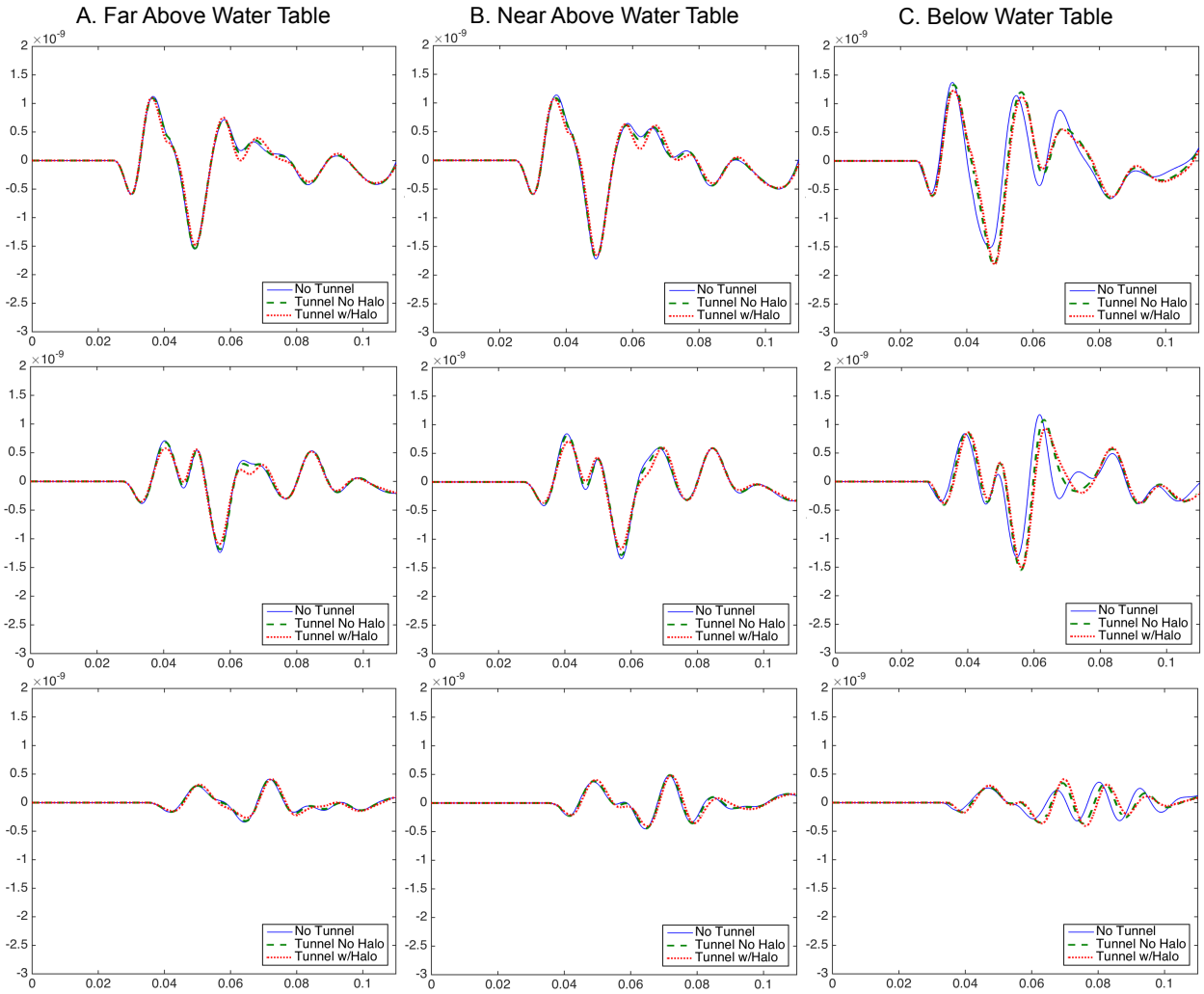

Figure 11. Single synthetic seismic traces for each of the three models (no tunnel, tunnel with no halo, and tunnel with halo) for each case relative to the water table (A, B, and C) where the tunnel is 14.5m deep. The top rows are seismic rays that have not passed through the tunnel or halo area. The middle rows are seismic rays that have passed through the tunnel (and halo) area where the receiver is relatively close to the tunnel. The bottom rows are seismic rays that have passed through the tunnel (and halo) area where the receiver is at a far offset from the tunnel.

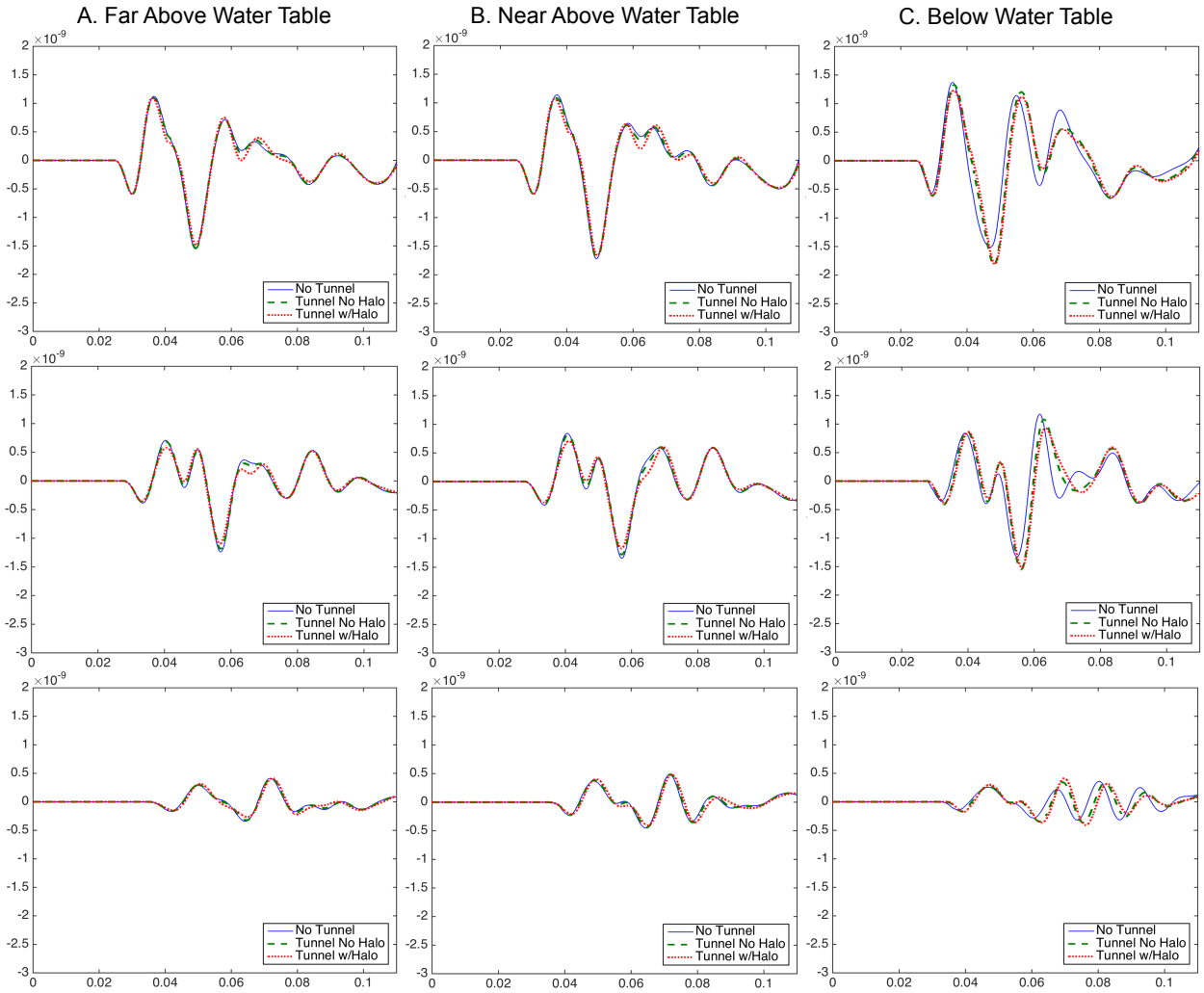

Figure 12. Single synthetic seismic traces for each of the three models (no tunnel, tunnel with no halo, and tunnel with halo) for each case relative to the water table (A, B, and C) where the tunnel is 7.5m deep. The top rows are seismic rays that have not passed through the tunnel or halo area. The middle rows are seismic rays that have passed through the tunnel (and halo) area where the receiver is relatively close to the tunnel. The bottom rows are seismic rays that have passed through the tunnel (and halo) area where the receiver is at a far offset from the tunnel.